Carbon-coated hierarchical NaTi$_2$(PO$_4$)$_3$ mesoporous microflowers with superior sodium storage performance

Chang Xu [a,1], Yanan Xu [a,1], Chunjuan Tang [a,b], Qiulong Wei [a], Jiashen Meng [a], Lei Huang [a], Liang Zhou [a,*], Guobin Zhang [a], Liang He [a], Liqiang Mai [a,*]

[a] State Key Laboratory of Advanced Technology for Materials Synthesis and Processing, Wuhan University of Technology, Wuhan 430070, PR China
[b] Department of Mathematics and Physics, Luoyang Institute of Science and Technology, Luoyang 471023, PR China

ABSTRACT

NASICON structured NaTi$_2$(PO$_4$)$_3$ with stable and open framework has become a promising electrode material for sodium-ion batteries. However, the intrinsic low electronic conductivity of NaTi$_2$(PO$_4$)$_3$ leads to inferior rate capability and poor active material utilization. Herein, we first report the synthesis of carbon-coated hierarchical NaTi$_2$(PO$_4$)$_3$ mesoporous microflowers (NTP/C-F), *via* a facile and controllable solvothermal method and subsequent annealing treatment. The unique structural features endow the NTP/C-F with excellent structural stability, enhanced charge transfer kinetics, and suppressed polarization. This architecture exhibits superior sodium storage performance: high initial capacity (125 mA h g^{-1} at 1 C), outstanding rate capability (95 mA h g^{-1} at 100 C), and ultra-long cycling stability (capacity retention of 77.3% after 10,000 cycles at 20 C). Time-resolved *in-situ* X-ray diffraction study reveals a typical two-phase electrochemical reaction with reversible structure change. This work suggests the integration of hierarchical structure and carbon coating provides a promising approach for boosting the electrochemical performances of battery electrode materials.

© 2016 Published by Elsevier Ltd.

1. Introduction

Developing new energy storage technologies plays an important role in current society because of the ever-growing energy demands and fossil-fuel shortage [1–4]. Using renewable and clean energy sources, such as solar, wind, and geothermal power, is a promising choice. Besides, the efficiency, stability, and safety of a power supply system should be significantly improved. Battery devices are an option [5,6]. Throughout the various battery technologies, lithium-ion batteries (LIBs) have covered a wide range of applications from portable electronics to (plug-in) hybrid electric vehicles due to its high energy density and long cycle life [7,8]. However, the potential increasing costs and limited resource for Li are detrimental to the future large-scale application [2,3]. Na with abundant reserves, low cost, and easy availability manifests similar physicochemical properties to Li [9,10]. Therefore, developing room-temperature sodium-ion batteries (SIBs) with a similar working principle to LIBs for large-scale applications is a reasonable alternative [7]. Searching for suitable electrode materials for SIBs is still a key point to realize green, high-efficiency and long-life rechargeable batteries nowadays [11].

Recently, the Na-superionic conductor (NASICON) structured compounds derived from polyanion system have been widely developed as potential active materials for SIBs and supercapacitors [9,12,13]. The NASICON structured compounds possess an open framework containing large interstitial channels, which can provide high ionic mobility [14,15]. Among these compounds, NaTi$_2$(PO$_4$)$_3$ (NTP) with high theoretical capacity, good thermal stability, low cost, and environmental compatibility has been considered as a promising electrode material for SIBs [16,17]. However, the NTP inevitably faces the intrinsic problems of low electronic conductivity and sluggish charge transfer kinetics, which result in poor cycling ability and inferior rate performance. Several approaches have been attempted to improve electron/ion transport kinetics of the NTP, *e.g.*, hybridizing with conductive additives [18–20], reducing the size of electrode materials [21–25]. Wu et al. synthesized porous NTP particles embedded in graphene network *via* two-step solvothermal processes combining with high-temperature calcination [18]. Benefiting from the good conductivity of graphene, the resulting composite shows an improved rate capability (67 mA h g^{-1} at 50 C) and cycling ability (1000 cycles at 10 C). Despite all the efforts, NTP with outstanding rate performance, ultra-long cycle life, and high capacity has rarely been realized.

Three-dimensional (3D) hierarchical micro/nanostructures have been applied in batteries in recent years to realize the
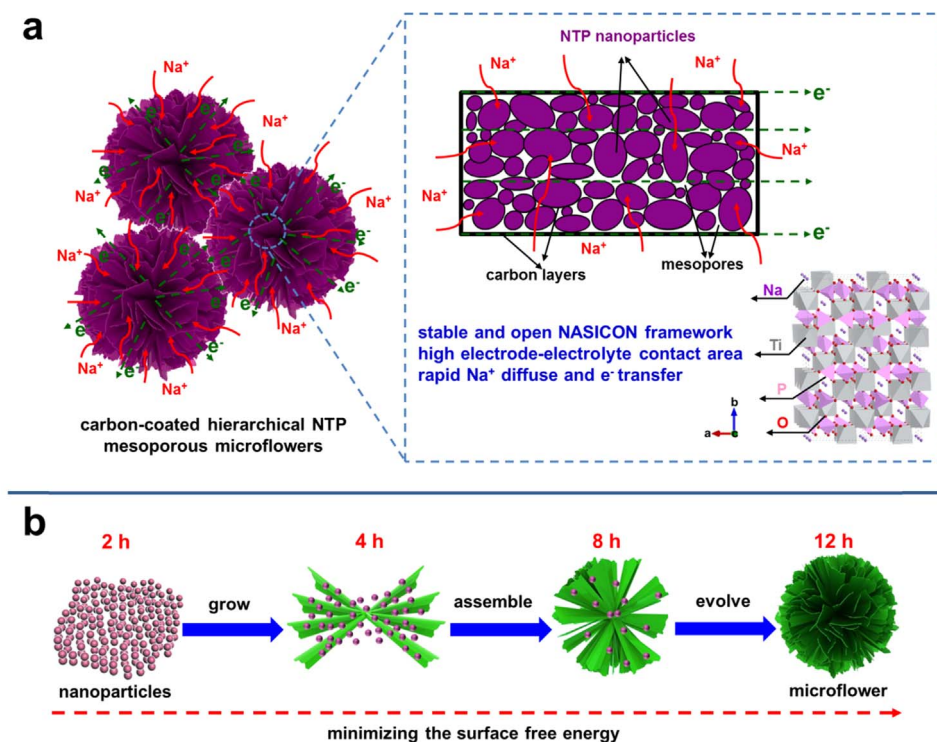
* Corresponding authors.
  E-mail addresses: liangzhou@whut.edu.cn (L. Zhou),
mlq518@whut.edu.cn (L. Mai).
  [1] These authors contributed equally to this work.

Fig. 1. (a) Schematic illustration of carbon-coated hierarchical $NaTi_2(PO_4)_3$ mesoporous microflowers with stable and open NASICON framework, high electrode-electrolyte contact area, and rapid Na^+ diffusion and e^- transfer. (b) Schematic illustration of the formation process for hierarchical flower-like precursors.

advantages of both nanosized building blocks and micro-meter sized assemblies [26–28]. The 3D hierarchical structures not only possess good structural stability and continuous ion/electron transfer, but also maintain reduced electron/ion diffusion length. However, the facile preparation of NTP with desirable hierarchical structures still remains a great challenge, probably due to its complicated crystal structure and multi-element composition.

Herein, we first present a facile and controllable synthesis of carbon-coated hierarchical $NaTi_2(PO_4)_3$ mesoporous microflowers (denoted as NTP/C-F). As schematically illustrated in Fig. 1a, the resultant NTP/C-F displays the following advantages: (a) stable and open NASICON framework; (b) mesoporous nanosheet-constructed hierarchical structure for high electrode-electrolyte contact area as well as short Na^+ and electron diffusion pathways; (c) the carbon skeleton for rapid electron transfer and structural stability improvement. As a SIB electrode, this architecture exhibits outstanding rate capability and ultra-long cycling stability. It delivers an initial capacity of 125 mA h g^{-1} at 1 C (1 C = 133 mA g^{-1}), realizing 93.7% of theoretical capacity. Even at an ultrahigh rate of 100 C (8 s for the full discharge/charge process), the reversible capacity still reaches 95 mA h g^{-1}. After 10,000 cycles at 20 C, the capacity retention is as high as 77.3% (85 mA h g^{-1}), superior to other reported NTP electrode materials in nonaqueous SIBs.

2. Experimental section

2.1. Material synthesis

Ethylene glycol (EG), tetrabutyl titanate (TBOT), $NaH_2PO_4 \cdot 2H_2O$, H_3PO_4 and glucose, of analytical grade, were purchased from the Sinopharm Chemical Reagent Co., Ltd. (Shanghai, China). First, TBOT (2 mmol) was slowly added into EG (20 mL) and vigorously stirred for 30 min to obtain a transparent solution. Then 0.1 M $NaH_2PO_4 \cdot 2H_2O$ (10 mL), H_3PO_4 (2 mmol), 0.1 M glucose (10 mL) were added into the above solution in sequence. The mixture was further stirred for 1 h to obtain a homogenous and transparent solution. After that, the obtained solution was transferred into a 50 mL Teflon-lined stainless steel autoclave and kept at 180 °C for 12 h. When the reaction completed, the system was cooled to room temperature naturally and dried at 120 °C. The brown powder precursors deposited at the bottom of the reactor were collected. Finally, NTP/C-F was obtained by preheating the precursor at 350 °C for 2 h followed by annealing at 700 °C for 4 h in Ar with a heating rate of 2 °C min^{-1}. The gel-like precursors gained at a solvothermal treatment time of 2 h were also subjected to annealing in Ar, while the other conditions were kept unchanged. Finally the carbon-coated NTP particles (denoted as NTP/C-P) were obtained.

2.2. Materials characterization

X-ray diffraction (XRD) measurements were performed to obtain the crystallographic information using a D8 Discover X-ray diffractometer with a nonmonochromated Cu Kα X-ray source. Field emission scanning electron microscopy (FESEM) images were collected with a JEOL-7100F microscope at an acceleration voltage of 10 kV. Energy dispersive X-ray spectra (EDS) element mappings were recorded by an Oxford IE250 system. Transmission electron microscopy (TEM) and high resolution TEM (HRTEM) images were recorded by a JEM-2100F STEM/EDS microscope. Brurauer–Emmerr–Teller (BET) surface areas were measured using a Tristar II 3020 instrument by adsorption of nitrogen at 77 K. Thermo gravimetric analysis (TGA) was conducted using a STA-449C. X-ray photoelectron spectrum (XPS) measurement was performed using a VG Multi Lab 2000 instrument. For in-situ XRD study, an electrochemical cell module with a beryllium window was used, while the slurry was directly cast on the beryllium window.

2.3. Measurement of electrochemical performance

The electrochemical measurements were carried out by assembling 2016 coin cells in a glove box filled with pure argon. Metallic sodium was used as the counter electrode. An appropriate amount of N-methyl-2-pyrrolidone (NMP) was used as the solvent to mix 70 wt% active material, 20 wt% carbon black with 10 wt% PVDF binder, then the slurry was coated on a Cu foil. After drying at 70 °C for 12 h, the electrode was dried in a vacuum oven for 4 h at 100 °C. The mass loading of active material in electrodes is around 1.8 mg cm^{-2}. The electrolyte was composed of 1 M NaClO$_4$ in the ethylene carbonate/dimethyl carbonate (1:1 w/w) with 5 wt% fluoroethylene carbonate (FEC) additive. The glass fiber (GF/D) from Whatman was used as the separator. The galvanostatic discharge-charge tests were carried out in a voltage window of 1.5–3.0 V on a battery test system (LAND CT2001A). The specific capacities were calculated based on the mass of NTP active material. Cyclic voltammetry (CV) and electrochemical impedance spectra (EIS) were tested with an electrochemical workstation (CHI 600e and Autolab PGSTAT 302N).

3. Results and discussion

The fabrication process of the NTP/C-F was illustrated in Fig. S1. EG was selected as the solvent to suppress the hydrolysis of TBOT. Aqueous solutions containing a certain amount of NaH$_2$PO$_4\cdot$2H$_2$O, H$_3$PO$_4$ and glucose were sequentially dropped into the above TBOT-EG solution to obtain a homogeneous solution. Solvothermal treatment of the resulting solution at 180 °C for 12 h led to the formation of hierarchical flower-like precursors (Fig. S2a). Time-dependent experiments under solvothermal conditions were conducted to elucidate the evolution process of hierarchical flower-like precursors. After a solvothermal treatment of 2 h, primary nanoparticles were formed (Fig. S3a, b). With a solvothermal reaction time of 3 h, the primary nanoparticles began to grow into intercrossed nanosheets due to the oriented attachment (Fig. S3c, d) [29]. The amount of intercrossed nanosheets further increased with the consumption of primary nanoparticles (Fig. S3e, f). As the solvothermal treatment increased to 8 h (Fig. S3g, h), nanosheets-constructed microflowers were formed to minimize the overall surface free energy [26,28,30]. Finally, hierarchical microflowers were entirely evolved as the solvothermal treatment extended to 12 h. The detailed formation process of hierarchical microflower precursors was schematically illustrated in Fig. 1b. The final NTP/C-F and NTP/C-P were prepared through annealing the precursors obtained at 12 h and 2 h at 700 °C, respectively.

XRD pattern (Fig. 2a) distinctly presents the crystallographic phase and crystallinity of NTP/C-F. All the diffraction peaks are accurately indexed to the NASICON structured NTP with R-3c space group (JCPDS no. 01-084-2010). The sharp and intense diffraction peaks suggest the well crystallized characteristic of NTP/C-F. The detailed morphology and structure of NTP/C-F are characterized by FESEM and TEM. The NTP/C-F well inherits the hierarchical microflower morphology of the precursors and the microflowers have an average diameter of ~ 5 μm (Fig. 2b–d). No obvious structure collapse is observed after annealing in Ar. Magnified FESEM images reveal that each individual microflower is composed of a number of intercrossed nanosheets. The nanosheet building blocks consist of numerous interconnected carbon-coated nanoparticles and obvious mesopores exist between the nanoparticles (Fig. 2e). The thickness of carbon layer coated on the surface of NTP nanocrystals is determined to be 2–5 nm. Different from the building blocks of NTP/C-F, the nanosheets of NTP/C-F precursor show a non-porous feature (Fig. S2b, c). It is thus speculated that the mesopores on NTP/C-F nanosheets come from the volatilization and carbonization of organic species during the annealing process [31,32]. The HRTEM image of NTP/C-F (Fig. 2f) clearly displays the lattice fringe of 4.3 Å, corresponding to the (110) crystal plane of rhombohedral NTP. EDS element mappings show that Na, Ti, P, O, and C distribute homogeneously in NTP/C-F (Fig. 2g). After etching the NTP from the NTP/C-F with hydrofluoric acid, a flower-like carbon skeleton can be obtained (Fig. S4), further confirming the uniform coating of carbon on the NTP surface.

XRD pattern of NTP/C-P (Fig. S5) also manifests high purity and crystallinity, similar to that of NTP/C-F. TEM and HRTEM images show that the NTP/C-P consists of irregular particles with amorphous carbon coating (Fig. S6a, b). Besides, the uniform distribution of Na, Ti, P, O, and C is also clearly observed from Fig. S6c.
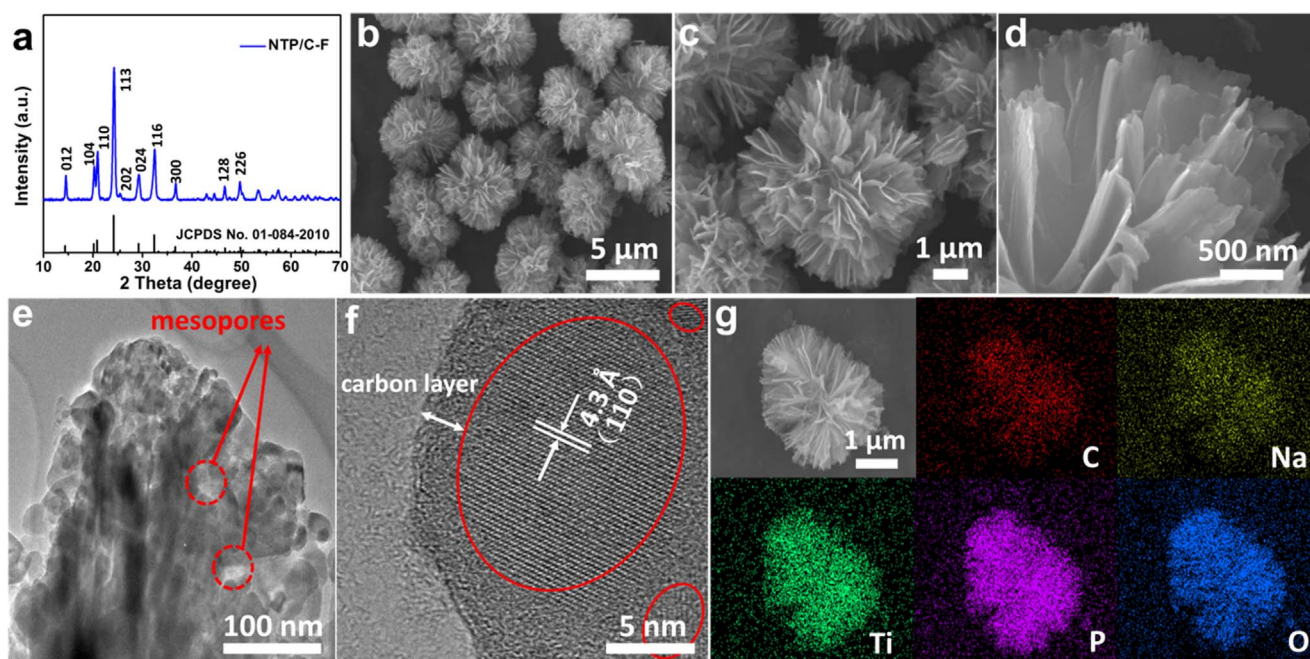

Fig. 2. (a) XRD pattern, (b–d) FESEM images, (e) TEM image, (f) HRTEM image, and (g) EDS elemental mappings of NTP/C-F.

Raman spectra are used to identify the nature of carbon on the surface of NTP/C-F and NTP/C-P (Fig. S7a). The two characteristic peaks located at ~1349 cm^{-1} and ~1595 cm^{-1} correspond to D-band (derived from disordered carbon) and G-band (graphitic carbon) [15,33]. The respective peak intensity ratio of the D band to G band (I_D/I_G) for NTP/C-F and NTP/C-P are around 1.04 and 1.05. Based on the TGA results, the carbon contents of NTP/C-F and NTP/C-P are determined to be 6.8 wt% and 13.6 wt%, respectively (Fig. S7b). The NTP/C-F possesses lower carbon content than NTP/C-P, which can be attributed to more complete decomposition of organic species during the longer solvothermal process. XPS is employed to probe the chemical state of Ti (Fig. S8). A single peak located at the binding energy of around 460.15 eV directly reflects the Ti^{4+} 2p3/2 oxidation state in the sample, which agrees with previous reports [25]. The pore size distributions and specific surface areas of the samples are investigated by nitrogen sorption (Fig. S9). The NTP/C-F presents a typical hysteresis loop at relatively high pressures (Fig. S9c), which is characteristic for mesoporous materials [31]. The BET surface area of NTP/C-F is measured to be 62.3 $m^2\,g^{-1}$. The Barrett-Joyner-Halenda (BJH) pore-size distribution of NTP/C-F (Fig. S9d) exhibits a broad pore size ranging from 3 to 30 nm. It's worth noting that the NTP/C-F precursor shows a low specific surface area (35.2 $m^2\,g^{-1}$) and no obvious mesopores (Fig. S9a, b), clearly testifying that the mesopores in nanosheets are generated during annealing. The relatively high BET surface area and large pore volume (0.11 $cm^3\,g^{-1}$) of NTP/C-F are beneficial for volume change accommodation, strain relaxation, and rapid Na^+ diffusion.

The electrochemical performances of NTP/C-F and NTP/C-P are investigated in a voltage window of 1.5–3.0 V *vs.* Na^+/Na. Because the discharge voltage of carbonaceous materials is below 1.0 V, the reversible capacity of carbon in the composites is negligible [24,33]. Fig. 3a exhibits the initial discharge-charge curves of NTP/C-F and NTP/C-P at 1 C. Both samples show coupled flat plateaus at around 2.1 V, corresponding to the redox reaction of Ti^{4+}/Ti^{3+}. Compared with NTP/C-P, the NTP/C-F delivers higher initial capacity (125 *vs.* 86 mA h g^{-1}) and smaller polarization (58 *vs.* 76 mV). After 200 cycles at 1 C (Fig. 3b), the NTP/C-F maintains a reversible specific capacity of 117 mA h g^{-1}. The rate performances of NTP/C-F and NTP/C-P are shown in Fig. 3c. Obviously, the NTP/C-F manifests higher and more stable capacity at each rate than NTP/C-P. At C-rates of 1, 2, 5, 10, 20, 30, and 50, the NTP/C-F delivers discharge capacities of 124, 120, 115, 111, 107, 102, and 100 mA h g^{-1}, respectively. Even at an ultrahigh rate of 100 C, the NTP/C-F still realizes a high specific capacity of 95 mA h g^{-1}, corresponding to 77% of the capacity obtained at 1 C. At such a high rate, the full discharge/charge process just takes 8 s. When the rate is returned to 1 C after high-rate cycling, the specific discharge capacity of the NTP/C-F recovers to 124 mA h g^{-1} again. The corresponding voltage profiles of the NTP/C-F at different rates from 1 to 100 C are
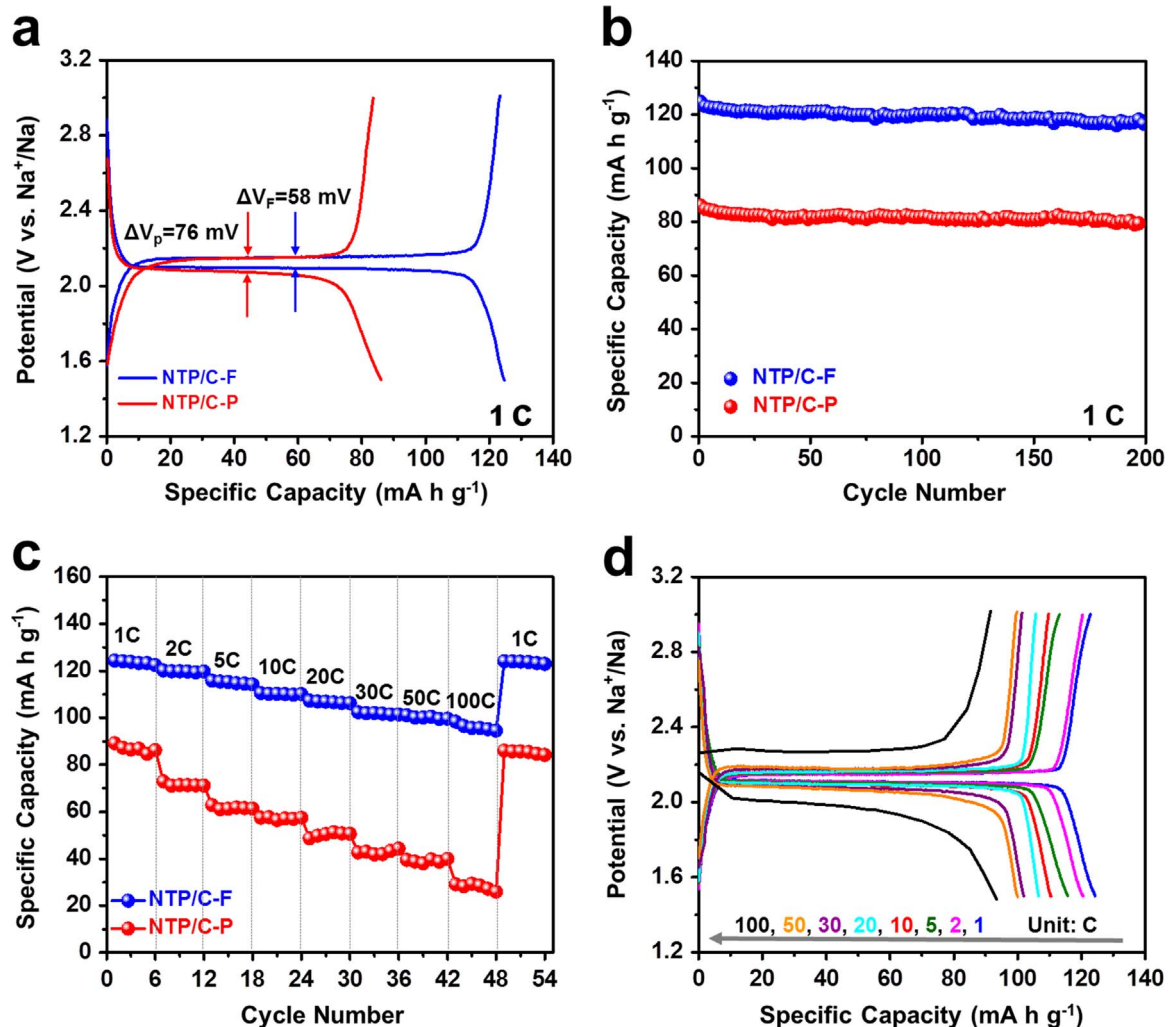

Fig. 3. (a) The initial discharge-charge curves of NTP/C-F and NTP/C-P at 1 C. (b) Cycling performances of NTP/C-F and NTP/C-P at 1 C. (c) The rate performances of NTP/C-F and NTP/C-P. (d) Discharge-charge curves of the NTP/C-F at different rates.
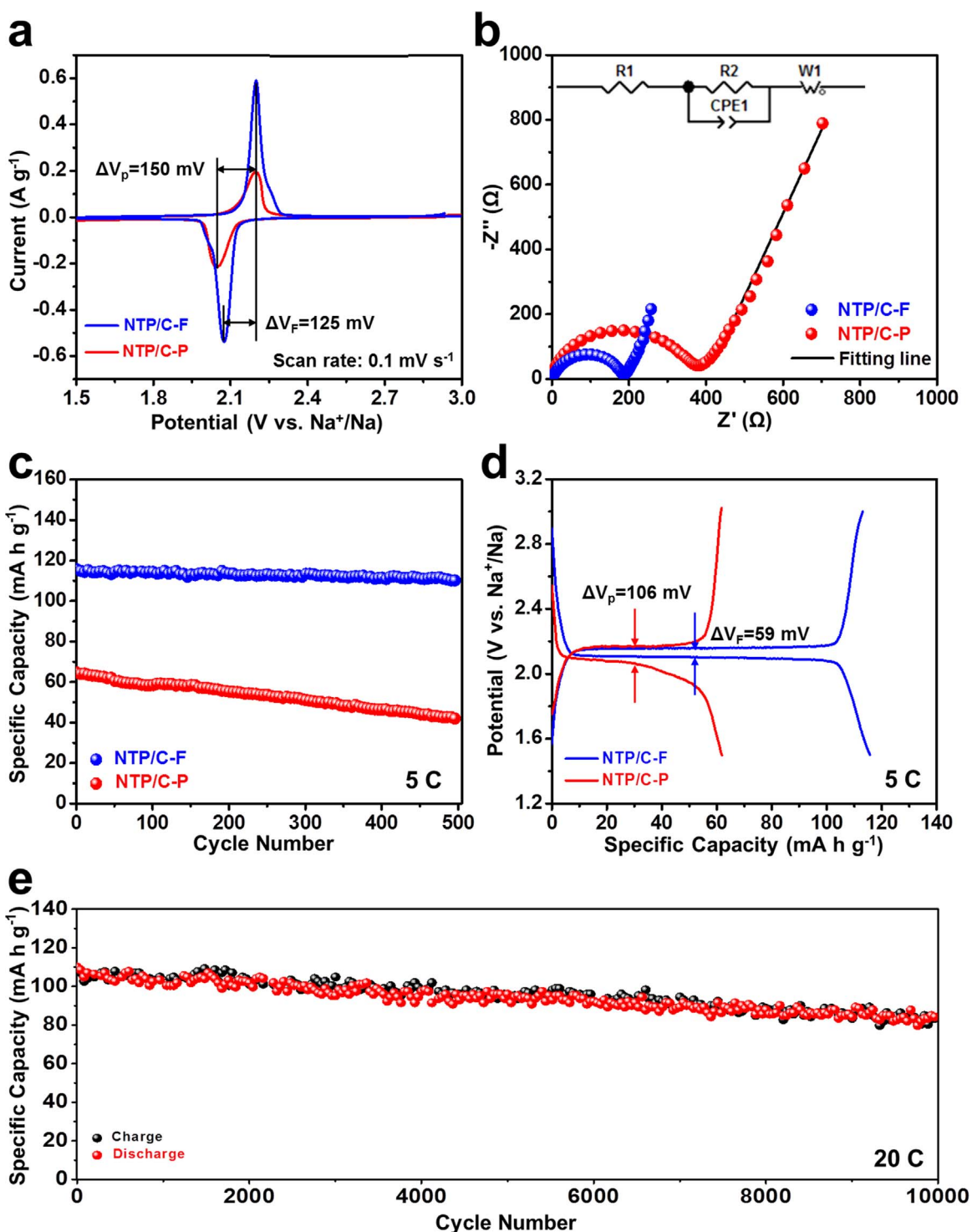
Fig. 4. (a) CV curves of NTP/C-F and NTP/C-P for the first cycle at a scanning rate of 0.1 mV s^{-1}. (b) The Nyquist plots of the fully charged NTP/C-F and NTP/C-P after initial cycle at 5 C with equivalent circuit inset. (c) Cycling performances and (d) the initial discharge-charge profiles of NTP/C-F and NTP/C-P at 5 C. (e) Ultralong cycling stability of the NTP/C-F for 10,000 cycles at 20 C.

displayed in Fig. 3d. Even at the high rate of 100 C, flat discharge-charge voltage plateaus with small polarization can be clearly discerned. In sharp contrast, the NTP/C-P shows high polarization and no obvious discharge-charge plateaus can be observed above 50 C (Fig. S10).

Fig. 4a exhibits the CV curves of NTP/C-F and NTP/C-P at a scan rate of 0.1 mV s^{-1}. Both samples have coupled peaks at around 2.2/2.05 V, agreeing well with the discharge-charge curves. Compared with NTP/C-P, the NTP/C-F shows more intense redox peaks,

higher peak areas, and lower overpotential (125 mV vs. 150 mV), suggesting its faster reaction kinetics and higher specific capacity. To reveal the reason of the enhanced electrochemical performance of NTP/C-F, the EIS measurement is carried out. The Nyquist plots (Fig. 4b) consist of a semicircle in the high-middle frequency range and a straight line in low frequency region. The semicircle represents charge transfer resistance (R_{ct}) between the electrolyte and electrode. Based on the equivalent circuit inset, the R_{ct} of NTP/C-F after the initial cycle at 5 C is determined to be 187 Ω, which is

much smaller than that of NTP/C-P (380 Ω). It indicates that the 3D hierarchical structure reduces the polarization and is beneficial to the efficient ion/electron transport between the electrode and electrolyte. Fig. 4c displays the cycling ability of both samples at 5 C. The NTP/C-F delivers a superior initial specific capacity of 116 mA h g^{-1} and retains a reversible capacity of 110 mA h g^{-1} after 500 cycles, corresponding to a capacity retention of 95%. For NTP/C-P, much inferior cycling performance is obtained. It only delivers an initial capacity of 65 mA h g^{-1} and low capacity retention of 64.9% after 500 cycles. The corresponding initial discharge-charge curves of both samples are shown in Fig. 4d. The polarization of NTP/C-P increases to 109 mV at 5 C, which is much larger than that of NTP/C-F (59 mV). Besides, the R$_{ct}$ of NTP/C-F after 500 cycles at 5 C changes slightly, while that of NTP/C-P surges to 836 Ω (Fig. S11). The EIS results unambiguously demonstrate the enhanced charge transfer kinetics of NTP/C-F upon cycling.

NTP/C-F also exhibits outstanding long-cycling performance at high rates. An initial reversible capacity of 114 mA h g^{-1} can be obtained at 10 C, retaining 101 mA h g^{-1} after 3000 cycles (Fig. S12a). The coulombic efficiency could keep at around 100% throughout cycling. Besides, selected discharge-charge curves of NTP/C-F at 10 C represent a tiny polarization change (Fig. S12b). At a higher C-rate of 20 C, the NTP/C-F still realizes a specific capacity of 110 mA h g^{-1} and a capacity retention of 77.3% after 10,000 cycles (Fig. 4e). The ultra-long cycling ability of NTP/C-F exceeds other reported results of NTP materials in nonaqueous SIBs (Table S1) [18,19,21,22,24]. The morphology of NTP/C-F after cycling is studied by SEM. Even after 5000 cycles at 20 C, the original hierarchical flowe-like morphology can be well maintained (Fig. S13), demonstrating its excellent structural stability.

To better reveal the enhanced sodium storage mechanism in the electrochemical performance of the NTP/C-F than NTP/C-P, time-resolved in-situ XRD technique is employed. For the in-situ XRD study, a clear variation in the selective regions of NTP/C-F and NTP/C-P is observed during galvanostatically discharged and charged at 50 mA g^{-1} in the voltage window of 1.5–3.0 V (Fig. 5). All of the diffraction patterns at the open circuit voltage state can be assigned to the rhombohedral NaTi$_2$(PO$_4$)$_3$ phase. For NTP/C-F, the peaks centered at 24.2°, 29.2°, and 32.4°, corresponding to the
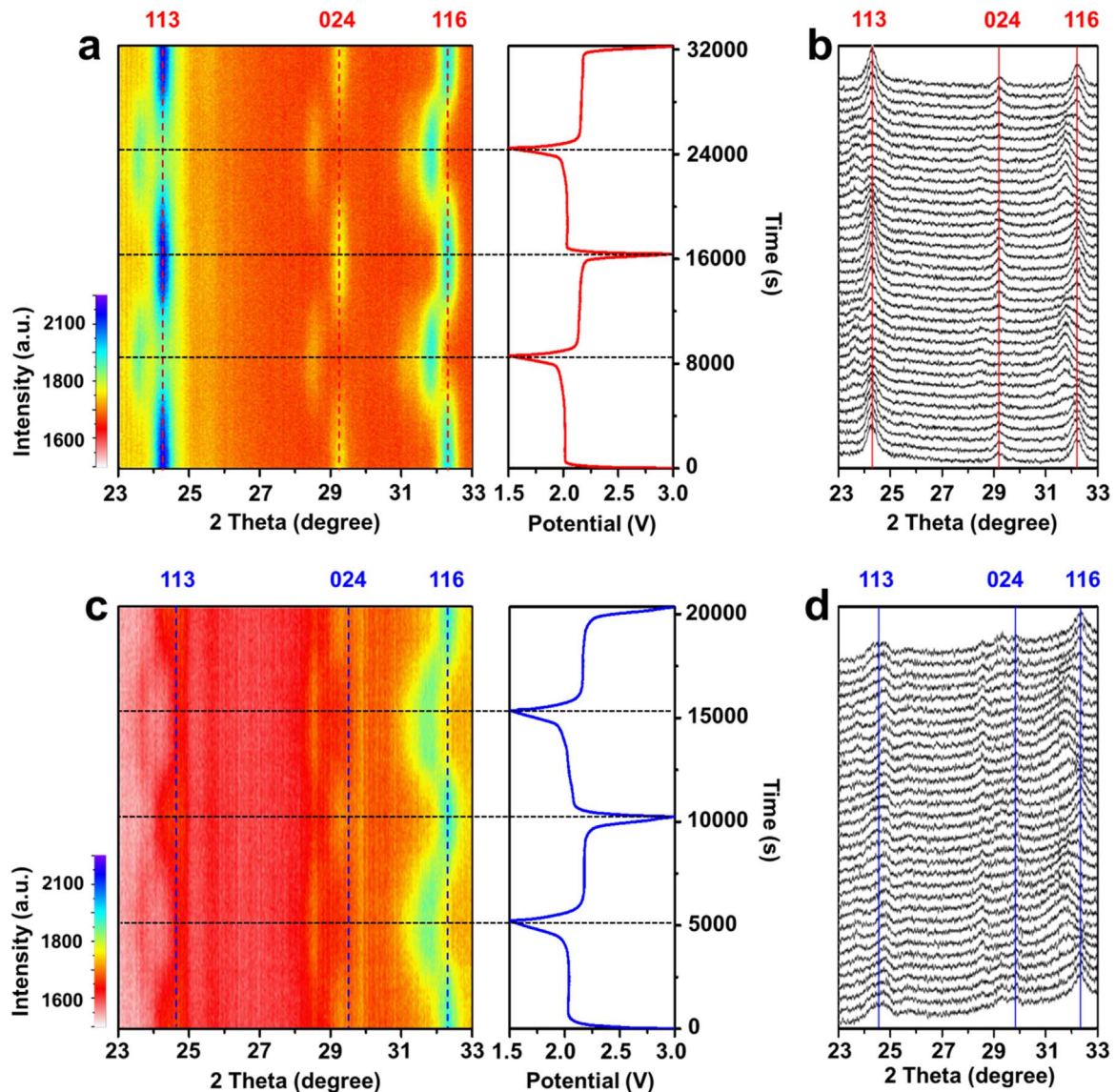

Fig. 5. *In-situ* XRD patterns of the NTP/C-F and NTP/C-P half cells during galvanostatic discharge and charge at 50 mA g^{-1} and a voltage range of 1.5–3.0 V: (a) the image plot of diffraction patterns and (b) selected individual diffraction patterns of the NTP/C-F stacked against the voltage profile at 23–33° during the first two discharge-charge cycles; (c) the image plot of diffraction patterns and (d) selected individual diffraction patterns of the NTP/C-P stacked against the voltage profile at 23–33° during the first two discharge-charge cycles.

(113), (024), and (116) diffractions of $NaTi_2(PO_4)_3$, gradually weaken on first discharge (Fig. 5a). With further sodiation, the reflections at 24.2°, 29.2°, and 32.4° disappear eventually along with the appearance and gradual enhancement of new diffractions at 23.5°, 28.5°, and 31.8°, revealing the formation of new phase [34]. At the end of discharge (1.5 V), the diffraction patterns can be indexed to $Na_3Ti_2(PO_4)_3$ [22,35,36]. The electrochemical process can be described as follows: $NaTi_2(PO_4)_3 + 2Na^+ + 2e^- \rightarrow Na_3Ti_2(PO_4)_3$. In the following charge process, the $Na_3Ti_2(PO_4)_3$ diffraction peaks decrease in intensity and disappear eventually; meanwhile, the (113), (024), and (116) peaks for $NaTi_2(PO_4)_3$ recover. It reflects a reversible extraction of Na^+. A closer monitor of selected individual diffraction patterns during the first two cycles stacked against the voltage profile is provided in Fig. 5b. The results suggest that (de)sodiation procedure of NTP/C-F occurs *via* the typical two-phase reaction [14,34]. The second discharge-charge process manifests the same trend, confirming the high reversibility of the two-phase electrochemical reaction for NTP/C-F. Compared with the distinct diffraction patterns of NTP/C-F, the peaks of NTP/C-P are wider and peak intensities are weaker, which reflect inferior crystallinity (Fig. 5c, d). For NTP/C-P, the (113) and (024) peaks of $NaTi_2(PO_4)_3$ still exist along with the appearance and enhancement of $Na_3Ti_2(PO_4)_3$ peaks on discharge; similarly, $Na_3Ti_2(PO_4)_3$ peaks do not disappear completely with the recover of $NaTi_2(PO_4)_3$ peaks on charge. The *in-situ* XRD study indicates that the active material utilization of NTP/C-P is lower than that of NTP/C-F during discharge-charge process.

The superior electrochemical performance of NTP/C-F can be attributed to the following factors: (1) the NASICON structured NTP possesses a highly stable and open framework, which is beneficial for rapid Na^+ diffusion and cycling stability; (2) the rich mesopores ensure not only intimate contact between liquid electrolyte and active $NaTi_2(PO_4)_3$ nanocrystals, but also short pathways for Na^+ and electron transport, which boosts the rate capability; (3) the carbon skeleton facilitates fast electron transfer and further prevents the structure from collapse and self-aggregation during long cycling. The synergistic effect of above-mentioned factors endows the NTP/C-F with excellent structural stability, enhanced charge transfer kinetics, and suppressed polarization. As a result, outstanding high-rate capability and ultra-long cycling stability can be achieved.

4. Conclusion

In summary, novel carbon-coated hierarchical $NaTi_2(PO_4)_3$ mesoporous microflowers have been firstly fabricated *via* a facile and controllable method. The unique structural features, such as stable and open NASICON structure, mesoporous nanosheet-constructed hierarchical architecture, and uniform carbon coating, endow the NTP/C-F with outstanding high-rate capability (95 mA h g^{-1} at 100 C) and ultra-long cycling stability (capacity retention of 77.3% after 10,000 cycles at 20 C). Time-resolved *in-situ* XRD study reveals a typical two-phase electrochemical reaction of NTP/C-F with reversible structure change. The above results demonstrate that NTP/C-F is a promising electrode material for high-performance SIBs.

Acknowledgments

Appendix A. Supporting information

Supplementary data associated with this article can be found in the online version at http://dx.doi.org/10.1016/j.nanoen.2016.08.026.

References

[1] D. Larcher, J. Tarascon, Nat. Chem. 7 (2015) 19–29.
[2] D. Kundu, E. Talaie, V. Duffort, L.F. Nazar, Angew. Chem. Int. Ed. 54 (2015) 3431–3448.
[3] M.D. Slater, D. Kim, E. Lee, C.S. Johnson, Adv. Funct. Mater. 23 (2013) 947–958.
[4] H. Pan, Y.-S. Hu, L. Chen, Energy Environ. Sci. 6 (2013) 2338–2360.
[5] Z. Yang, J. Zhang, M.C. Kintner-Meyer, X. Lu, D. Choi, J.P. Lemmon, J. Liu, Chem. Rev. 111 (2011) 3577–3613.
[6] B. Dunn, H. Kamath, J.-M. Tarascon, Science 334 (2011) 928–935.
[7] S.W. Kim, D.H. Seo, X. Ma, G. Ceder, K. Kang, Adv. Energy Mater. 2 (2012) 710–721.
[8] L.P. Wang, L. Yu, X. Wang, M. Srinivasan, Z.J. Xu, J. Mater. Chem. A 3 (2015) 9353–9378.
[9] V. Palomares, P. Serras, I. Villaluenga, K.B. Hueso, J. Carretero-González, T. Rojo, Energy Environ. Sci. 5 (2012) 5884–5901.
[10] Z. Jian, L. Zhao, H. Pan, Y.-S. Hu, H. Li, W. Chen, L. Chen, Electrochem. Commun. 14 (2012) 86–89.
[11] N. Yabuuchi, K. Kubota, M. Dahbi, S. Komaba, Chem. Rev. 114 (2014) 11636–11682.
[12] C. Masquelier, L. Croguennec, Chem. Rev. 113 (2013) 6552–6591.
[13] Z. Jian, V. Raju, Z. Li, Z. Xing, Y.S. Hu, X. Ji, Adv. Funct. Mater. 25 (2015) 5778–5785.
[14] Z. Jian, W. Han, X. Lu, H. Yang, Y.S. Hu, J. Zhou, Z. Zhou, J. Li, W. Chen, D. Chen, Adv. Energy Mater. 3 (2013) 156–160.
[15] Y. Fang, L. Xiao, X. Ai, Y. Cao, H. Yang, Adv. Mater. 27 (2015) 5895–5900.
[16] C. Delmas, F. Cherkaoui, A. Nadiri, P. Hagenmuller, Mater. Res. Bull. 22 (1987) 631–639.
[17] Z. Li, D. Young, K. Xiang, W.C. Carter, Y.M. Chiang, Adv. Energy Mater. 3 (2013) 290–294.
[18] C. Wu, P. Kopold, Y.-L. Ding, P.A. van Aken, J. Maier, ACS Nano 9 (2015) 6610–6618.
[19] J. Yang, H. Wang, P. Hu, J. Qi, L. Guo, L. Wang, Small 11 (2015) 3744–3749.
[20] W. Wu, J. Yan, A. Wise, A. Rutt, J. Whitacre, J. Electrochem. Soc. 161 (2014) A561–A567.
[21] G. Pang, P. Nie, C. Yuan, L. Shen, X. Zhang, H. Li, C. Zhang, J. Mater. Chem. A 2 (2014) 20659–20666.
[22] G. Yang, H. Song, M.W.C. Wang, J. Mater. Chem. A 3 (2015) 18718–18726.
[23] Y. Jiang, J. Shi, M. Wang, L. Zeng, L. Gu, Y. Yu, ACS Appl. Mater. Interfaces 8 (2016) 689–695.
[24] Y. Jiang, L. Zeng, J. Wang, W. Li, F. Pan, Y. Yu, Nanoscale 7 (2015) 14723–14729.
[25] D. Wang, Q. Liu, C. Chen, M. Li, X. Meng, X. Bie, Y. Wei, Y. Huang, F. Du, C. Wang, ACS Appl. Mater. Interfaces 8 (2016) 2238–2246.
[26] A.Q. Pan, H.B. Wu, L. Zhang, X.W. Lou, Energy Environ. Sci. 6 (2013) 1476–1479.
[27] Y. Sun, X. Hu, C.Y. Jimmy, Q. Li, W. Luo, L. Yuan, W. Zhang, Y. Huang, Energy Environ. Sci. 4 (2011) 2870–2877.
[28] C. Sun, S. Rajasekhara, J.B. Goodenough, F. Zhou, J. Am. Chem. Soc. 133 (2011) 2132–2135.
[29] Y. Li, J. Liu, X. Huang, G. Li, Cryst. Growth Des. 7 (2007) 1350–1355.
[30] Q. Wang, W. Zhang, Z. Yang, S. Weng, Z. Jin, J. Power Sources 196 (2011) 10176–10182.
[31] W. Li, F. Zhang, Y. Dou, Z. Wu, H. Liu, X. Qian, D. Gu, Y. Xia, B. Tu, D. Zhao, Adv. Energy Mater. 1 (2011) 382–386.
[32] Q. Li, Q. Wei, J. Sheng, M. Yan, L. Zhou, W. Luo, R. Sun, L. Mai, Adv. Sci. 2 (2015) 1500284.

[33] C. Bommier, T.W. Surta, M. Dolgos, X. Ji, Nano Lett. 15 (2015) 5888–5892.
[34] P. Senguttuvan, G. Rousse, M. Arroyo y de Dompablo, H. Vezin, J.-M. Tarascon, M. Palacín, J. Am. Chem. Soc. 135 (2013) 3897–3903.
[35] Z. Li, D.B. Ravnsbæk, K. Xiang, Y.-M. Chiang, Electrochem. Commun. 44 (2014) 12–15.
[36] H. Liu, F.C. Strobridge, O.J. Borkiewicz, K.M. Wiaderek, K.W. Chapman, P.J. Chupas, C.P. Grey, Science 344 (2014) 1451–1452.

Chang Xu is now a postgraduate student at Wuhan University of Technology. She has joined WUT-Harvard Joint Nano Key Laboratory for two years. Her current research focuses on energy storage nanomaterials and devices.

Yanan Xu received his B.S. degree in Department of Materials Science of Engineering from Wuhan University of Technology in 2013. He is currently working toward the Ph.D. degree. His current research involves the nanomaterials achieving high energy density and power density for lithium ion battery, sodium ion battery and magnesium ion battery.

Chunjuan Tang received her Ph.D. degree in Chinese Academy of Sciences in 2008. She has worked in Luoyang Institute of Science and Technology as an associate professor since 2012. Now she is a postdoctor in Wuhan University of Technology, whose interests focus on energy storage.

Qiulong Wei. received his Ph.D. degree from Wuhan University of Technology in 2016. Now, he is a postdoctoral fellow with Prof. Bruce Dunn at University of California Los Angeles. His current research involves the design and synthesis of novel nanomaterials for achieving both high energy density and power density electrochemical energy storage device, including the lithium-ion battery, sodium-ion battery and the hybrid capacitor.

Jiashen Meng received his B.S. degree from Wuhan University of Technology in 2015. He is currently working toward the Ph.D. degree in Wuhan University of Technology and his current research focuses on the energy storage and conversion materials.

Lei Huang received his B.S. degree in Department of Materials Science of Engineering from Wuhan University of Technology in 2014. He is currently a postgraduate student at Wuhan University of Technology. His current research involves nanoenergy materials and devices.

Liang Zhou received his B.S. (2006) and Ph.D. (2011) from Fudan University (with Prof. Dongyuan Zhao and Prof. Chengzhong Yu). He then carried out postdoctoral research in Prof. Xiong Wen (David) Lou's group at Nanyang Technological University and Prof. Chengzhong Yu's group at The University of Queensland. He is currently a Professor at Wuhan University of Technology. His research interests are focusing on functional nanomaterials for energy storage and conversion applications.

Guobin Zhang received his B.S. degree in Inorganic Non-metallic Materials Engineering from Inner Mongolia University of Science & Technology in 2014 and he is currently working toward the ph.D. degree. His current research interests include nanomaterials for Li-ions batteries, supercapacitors, sodium batteries and *in-situ* characterization.

Liang He is an associate professor of the State Key Laboratory of Advanced Technology for Materials Synthesis and Processing at Wuhan University of Technology. He received his Ph.D. degree from Tohoku University (Japan) in 2013. His current research interests include the microfabrication and characterizations of micro/nanostructures and devices for applications in MEMS (Micro Electro Mechanical Systems).

Liqiang Mai is a Chair Professor of Materials Science and Engineering at Wuhan University of Technology (WUT). He received his Ph.D. from WUT in 2004. He carried out his postdoctoral research in the laboratory of Prof. Zhonglin Wang at Georgia Institute of Technology in 2006–2007 and worked as advanced research scholar in the laboratory of Prof. Charles M. Lieber at Harvard University in 2008–2011. His current research interests focus on nanowire materials and devices for energy storage. He is the winner of the National Natural Science Fund for Distinguished Young Scholars, China Youth Science and Technology Award, Guanghua Engineering Award, and so forth.